

SUMAMPS-based Gain Maps for the HRC-I

Jennifer Posson-Brown & Vinay Kashyap

November 2009

Abstract

For both the HRC-I and HRC-S, the scaled sum of amplifier signals (SUMAMPS) is a better proxy for spectral response than the PHA. Here we discuss the creation of a set of time-dependent gain maps for the HRC-I based on and for use with scaled SUMAMPS. Using observations of AR Lac, G21.5-0.9 and HZ 43 taken regularly since launch, we model corrections for the spatial and temporal gain changes. The resulting time-dependent gain maps convert scaled SUMAMPS into "SUMAMPS pulse invariant" (SPI), allowing for comparison of source profiles taken at different epochs or locations on the detector.

1 Introduction

The gain of the HRC-I has declined since launch (Posson-Brown & Donnelly 2003, Wilton 2005, Posson-Brown & Kashyap 2007). To address this gain decline, we made a series of time-dependent gain correction maps, which were released in CALDB 3.3.0 (Posson-Brown & Kashyap 2007). In this memo we describe the creation of a new set of time-dependent gain maps. This set differs from the previous set in two ways. First, the maps are based on (and intended for use with) scaled SUMAMPS instead of PHA.¹ Second, we correct for the time dependence of the gain decline with an inverse exponential plus linear function fit to temporal correction factors derived from AR Lac, G21.5-0.9 and HZ 43, instead of a pure linear function fit to the median AR Lac PHAs.

In Section 2 we review the observations used to create the maps and our data processing steps. We introduce scaled SUMAMPS in Section 3. The gain correction process is described in Section 4. First, in Section 4.1, we discuss the creation of the initial gain map from pre-flight lab data. Next, we review the corrections for the spatial gain variations (Section 4.2), derived from observations of AR Lac. Finally, in Section 4.3, we explain the temporal correction, based on observations of AR Lac, HZ 43, and G21.5-0.9. In Section 4.4 we test the new gain maps on several calibration observations. We summarize in Section 5.

2 Observations and Data Reduction

2.1 AR Lac

Yearly calibration observations of the RS CVn binary AR Lac are taken at 21 locations on the detector to monitor the gain response of the HRC-I. The locations of the pointings are shown in Figure 1. Each observation is nominally 1 ks long but effective observation times may be shorter because of background flares. The ObsIDs for all observations used in this analysis are listed in Tables 1 and 2, along with the deadtime and effective (post-filtering) exposure time.

¹Starting with CIAO 4.2, `hrc_process_events` will replace PHA-based PI with SUMAMPS-based PI by default. The capability to generate PHA-based PI will not be immediately eliminated, though it will be depreciated.

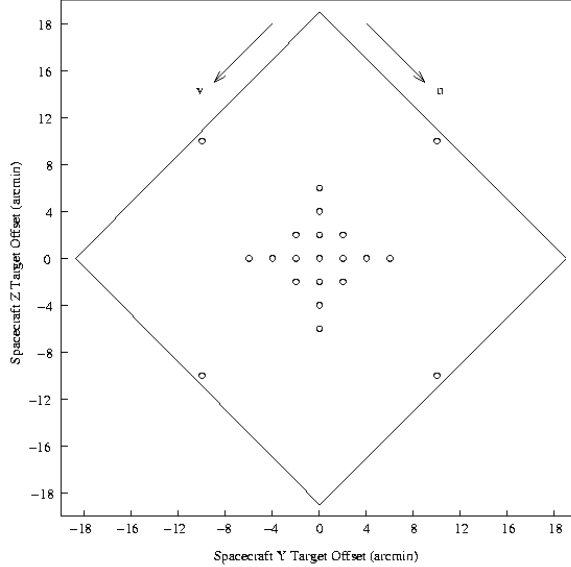


Figure 1: Locations of AR Lac observations on the HRC-I. Calibration observations are carried out at the aimpoint and 20 offset locations each cycle in order to monitor the gain: $(Y_{\text{sim}}, Z_{\text{sim}}) = (0', 0'), (0', \pm 2'), (\pm 2', 0'), (\pm 2', \pm 2'), (0', \pm 4'), (\pm 4', 0'), (0', \pm 6'), (\pm 6', 0'),$ and $(\pm 10', \pm 10')$

2.2 G21.5-0.9 and HZ 43

SNR G21.5-0.9 and white dwarf HZ 43 are observed regularly with the HRC-I at the detector aimpoint. We use these observations, along with AR Lac, to determine the temporal correction (Section 4.3). The ObsIDs, dates, exposure times, and deadtime corrections for these observations are given in Tables 3 and 4.

2.3 Data Processing

Our data processing methods are described in detail in Posson-Brown & Kashyap (2007). We will briefly review them here. We reduce the data with CIAO (4.1; CALDB 4.1) and analyze the data with pre-packaged and custom-built IDL routines (e.g., PINTofALE; Kashyap & Drake 2000). For each observation, we reprocess the Level 1 event list with `hrc_process_events` using the newest calibration products and no gain correction (`gainfile=NONE`). We filter on the default GTI and also exclude times when the detector-wide event rate exceeds 150 ct s^{-1} (safely under the telemetry saturation limit of 184 ct s^{-1}).²

For AR Lac, we extract source events from an 800×800 pixel box centered on the nominal observation location in chip coordinates. Background is estimated by collecting the events in the same location from the 20 other observations carried out in that cycle. The background counts are normalized by their appropriate exposure times prior to subtracting them from the source counts. For HZ 43 and G21.5-0.9, we extract source counts from a circular region around the aimpoint (using radii of $1.5''$ and $45''$ in sky coordinates, respectively) and background counts from nearby regions.

For the previous set of gain maps (Posson-Brown & Kashyap 2007) we calculated the median PHA value for each observation. Here, we use the mean scaled SUMAMPS value (see §3).

²For the Oct 99 AR Lac observations done in conjunction with the HRC-I voltage adjustment, we use a set of GTIs based on when the voltage was stable at the low setting (Juda, private communication) in place of the default GTIs.

3 Scaled SUMAMPS

The nominal gain metric for the HRC is Pulse Height Amplitude (PHA), which is the sum of all detector amplifier signals. However, on the HRC-S, PHAs vary largely over small spatial scales on the detector, while an alternate metric, SUMAMPS, shows much less spatial variation (Wargelin 2008). Furthermore, for both the HRC-I and HRC-S, the PHA values are limited by saturation at PHA=255, while SUMAMPS are not, and thus provide a better capability for spectral discrimination. The SUMAMPS value for an event is the sum of the signals from the three amplifiers nearest the event signal on each axis (i.e. AU1, AU2, AU3, and AV1, AV2, AV3) and is given in the Level 1 event list.³

Due to the superiority of SUMAMPS for gain measurements on the HRC, the HRC calibration team decided to switch from PHA to scaled SUMAMPS (“SAMP”) as the standard gain measure. The scaling is done by the amplifier scale factor value (AMP_SF) as follows:

$$SAMP = \frac{SUMAMPS \times 2^{AMP_SF-1}}{C} \quad (1)$$

where C is a constant. For the HRC-S, $C = 128$ (Wargelin 2008). For the HRC-I, we chose $C = 148$. This value was chosen so that the resulting SAMPs would match PHA values closely. Figure 2 shows the SAMP and PHA profiles for an observation of AR Lac done at the HRC-I aimpoint. Note that the profiles are very similar but for channel 255. PHA is restricted to 256 channels (0 - 255), so high energy events pile-up in channel 255. However, we have allowed for 1024 SAMP channels, so there is no pile-up. Thus, SAMP contains more information than PHA about high energy events. For the HRC-I, this is the only significant difference between SAMP and PHA. (Unlike the HRC-S, neither gain metric shows strong small-scale spatial variations.)

Figure 3 shows a scatter plot of mean PHA versus mean SAMP values for HRC-I/LETG observations of HR1099, PKS2155-304, and Cygnus X-2. Each data point shows the mean of the total background-subtracted PHA or SAMP profile for events in a given wavelength bin. (The wavelength bins are nonuniform in size and were set so that each contains at least 2000 counts.) The solid blue line shows a linear fit to the data between PHA=140:160. Note that the best-fit slope is nearly one and the best-fit offset nearly zero, indicating that the mean SAMP tracks the mean PHA very well in this range.

Finally, Figure 4 shows the ratio of median SAMP to median PHA for the AR Lac observations used to construct the time-dependent gain maps. Note that the median SAMP and PHA are equal to within roughly $\pm 5\%$.

Since SAMP and PHA are similar for the HRC-I, it is not surprising that, like PHA, SAMP values reveal the gain decline that has occurred since launch. Figure 5 shows the mean SAMP values for all 21 observation locations on the detector, with a different plotting symbol for each epoch. At all locations, the mean is declining with time. This is nearly identical to what we see with PHA (cf. Figure 2 in Posson-Brown & Kashyap 2007).

4 Time Dependent Gain Correction

In order to calculate time-independent SAMP pulse invariant (SPI) values, we carry out corrections to SAMP in two stages, computing the spatial and temporal gain corrections independently as we did previously for the PHA maps (Posson-Brown & Kashyap 2007).

³Note that the values of AU3 and AV3 in the Level 1 event list are *not* tap-ringing corrected. However, SUMAMPS in the Level 1 event list is calculated with the tap-ringing corrected values of AU3 and AV3.

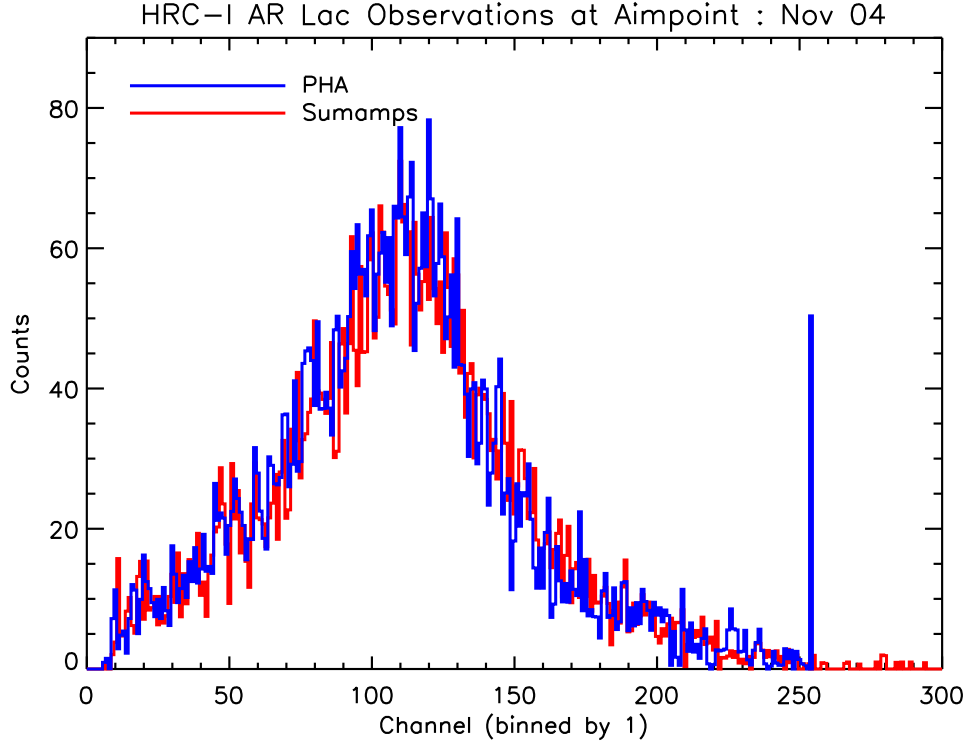


Figure 2: A comparison of PHA and SAMP profiles for HRC-I AR Lac ObsID 4294. Note that the profiles are very similar, except for PHA saturating at channel 255.

At each observation epoch, the SAMP are multiplied by a gain correction surface $g(\vec{x}|t)$ that carries out a “flat-fielding” of the SAMP values, i.e., at each epoch the SAMP at location \vec{x} are transformed to match the SAMP at the aimpoint location. After this “flat-fielding”, the SAMP are no longer a function of \vec{x} , and thus will be denoted $\text{SAMP}(\vec{0}|t)$. A time dependent correction, $TC(t)$ is then applied to $\text{SAMP}(\vec{0}|t)$ to transform them to pulse-invariant SAMP (SPI).

Thus,

$$\text{SPI} = \text{SAMP}(\vec{x}, t) \times g(\vec{x}|t) \times TC(t) \equiv \text{SAMP}(\vec{0}|t) \times TC(t) \quad (2)$$

4.1 Lab Map

The HRC-I gain response was measured during pre-flight ground calibration with a series of flat field maps at six energies spanning 0.183–6.404 keV (Wilton 2005). For each energy, we create a SAMP gain map by calculating the mean SAMP for events in half-tap (128 x 128 physical pixel) bins. We average these six maps, then normalize the resulting map to its mean central value, calculated from the central 5x5 taps (10x10 image pixels).⁴ Finally, we take the reciprocal of this map, since the gain correction is applied as a multiplicative factor in `hrc_process_events`. This “pre-flight” map, $g_{\text{LAB}}(\vec{x})$, is shown in Figure 6. (The map is set to 1 in the inactive region around the edges of the detector.)

⁴Note that the previous PHA-based lab map was normalized to the central ninth of the detector (Wilton 2005) – a much larger region than the central 5x5 taps used to normalize the SAMP-based map. As a result, the values in the SAMP-based map are greater than those in the PHA-based map, so SPI values will be consistently larger than PI values for a given observation.

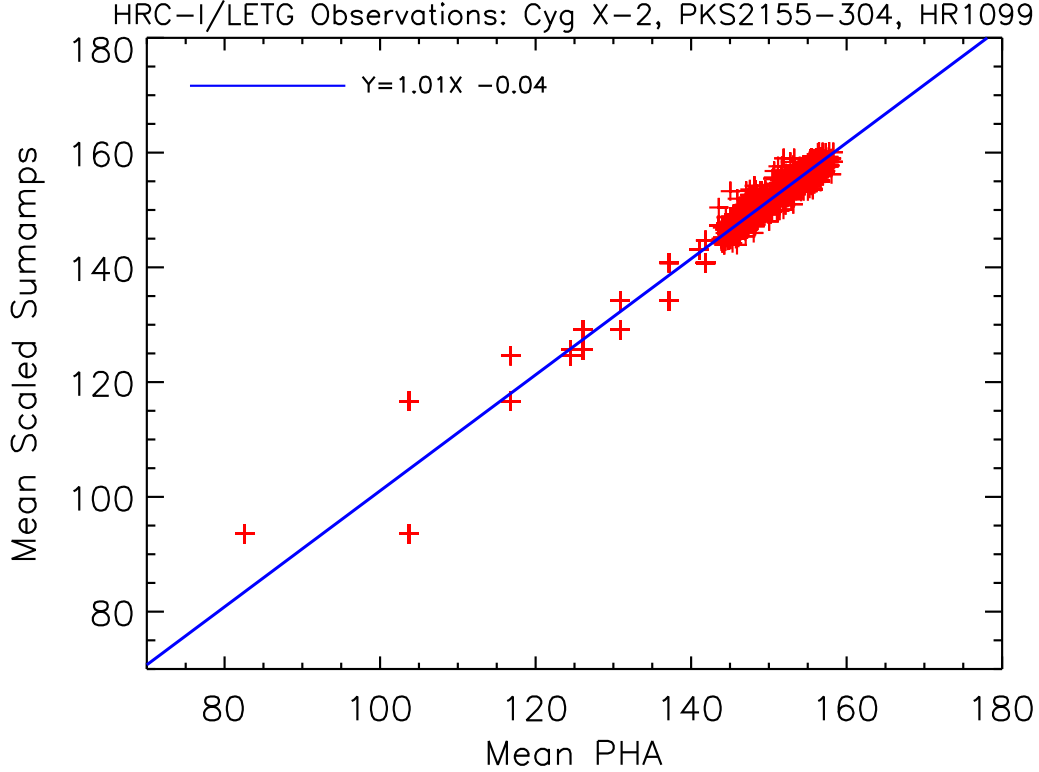


Figure 3: Mean PHA vs mean SAMP for several sources (HR1099, PKS2155-304, and Cygnus X-2) observed with HRC-I/LETG. Each point represents the background-subtracted mean of the combined profile in a given wavelength bin. The nonuniform wavelength bins are such that each bin contains at least 2000 counts. The solid blue line shows a linear fit to the data between PHA=140:160. Note that the best-fit slope ≈ 1 and the best-fit offset ≈ 0 indicating that the mean SAMP tracks the mean PHA very well in this range.

4.2 Spatial Corrections

We correct for the spatial variations in gain response by creating a series of correction maps $g(\vec{x}|t)$, one per epoch. Each map is a modification of the high-resolution lab gain correction map $g_{\text{LAB}}(\vec{x})$, described in the previous section, by correction factors γ which are determined at each of the 21 observation locations. A smooth surface is fit to these correction factors, and the gain correction map at that epoch is derived as

$$g(\vec{x}|t) = g_{\text{LAB}}(\vec{x}) \times \gamma(\vec{x}|t) \quad (3)$$

This procedure preserves the high spatial resolution present in the lab calibration data, while accounting for the gross changes that have occurred in the gain since launch.

The corrective factors γ are computed by a direct comparison of the spectra at different pointings to the aimpoint spectrum. This method was described in detail in Posson-Brown & Kashyap (2007) and we will review it briefly here.

First, putative spatially gain-corrected SAMPs are computed as

$$\text{SAMP}_{\text{LAB}}(\vec{x}, t) = \text{SAMP}(\vec{x}, t) \cdot g_{\text{LAB}}(\vec{x}). \quad (4)$$

These modified SAMPs are binned into spectra $f(\text{SAMP})$, and the value of γ that results in the best match between $f(\gamma \cdot \text{SAMP}_{\text{LAB}}(\vec{x}, t))$ and $f(\text{PHA}_{\text{LAB}}(\text{aim}, t))$ is determined via a grid-search over γ

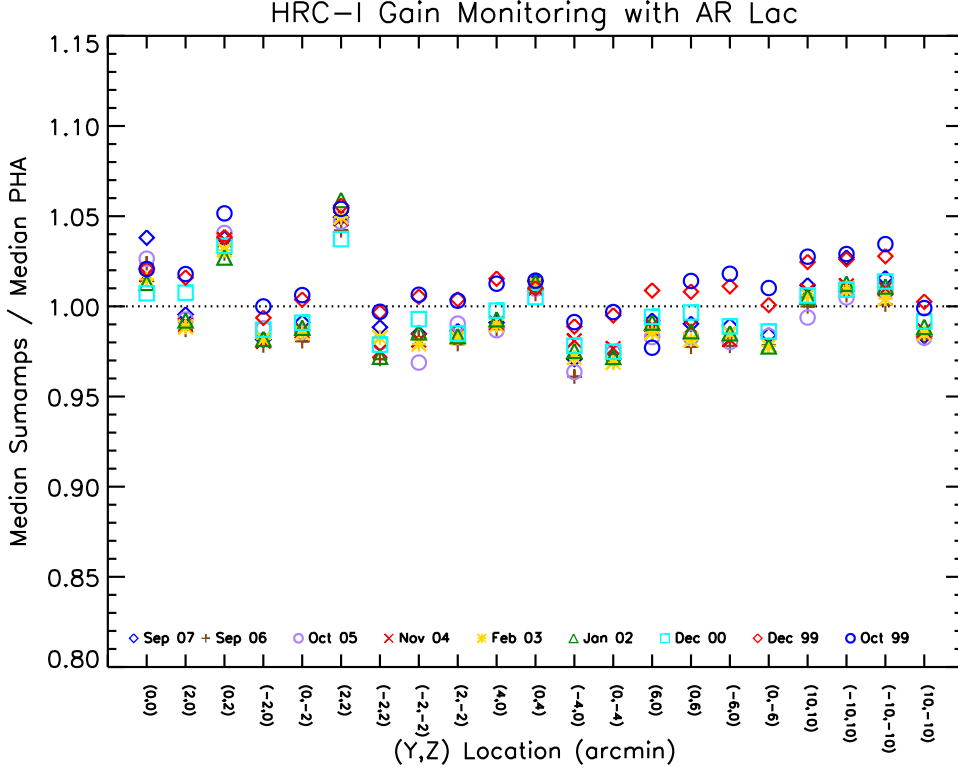


Figure 4: Ratio of median SAMP to median PHA for all AR Lac observations.

that minimizes the χ^2 value between the two counts histograms.

The resulting correction factors are shown in Figure 7. We use them to interpolate a minimum curvature surface at all locations over the detector to obtain the corrective surface $\gamma(\vec{x}|t)$ for each epoch. This is multiplied by the high-resolution gain map $g_{\text{LAB}}(\vec{x})$ to obtain the gain correction map $g(\vec{x}|t)$ for the epoch (Equation 3).

We test the spatial gain correction maps by independently applying $g(\vec{x}|t)$ to the $\text{SAMP}(\vec{x},t)$ values and comparing the mean $\text{SAMP}(\vec{0}|t)$ for all data sets. The results are shown in Figure 8. As expected, the means for each epoch are uniform, i.e., the gain correction has removed the spatial dependence in the $\text{SAMP}(\vec{x},t)$. Note that these maps are intermediate products, and are not available in the Calibration Database.

4.3 Temporal Correction

Having made correction maps for the spatial non-uniformity of the detector response, our next task is to correct for the time dependence of the gain decline. We seek to calculate the temporal correction as a function of time only, and then apply it to the gain correction map for each epoch ($g(\vec{x}|t)$, see §4.2) as a multiplicative factor (see Equation 2). That is, we want to find a temporal correction function (TC) such that

$$SPI = \text{SAMP}(\vec{0}|t) \times TC(t), \quad (5)$$

where t is the time since October 1999, SPI is the spatially and temporally invariant SAMP, and $\text{SAMP}(\vec{0}|t)$ are the “flat-field” SAMP values.

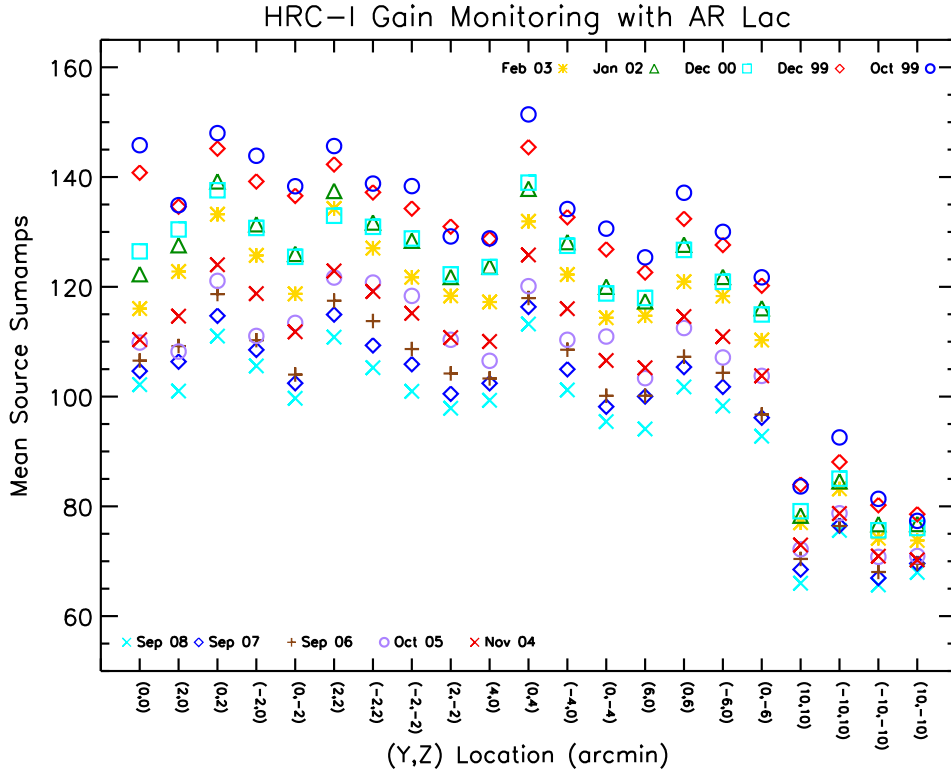


Figure 5: Mean background-subtracted SAMP as a function of observation location, with different plotting symbols showing different epochs. Note that at all locations, the mean declines with time.

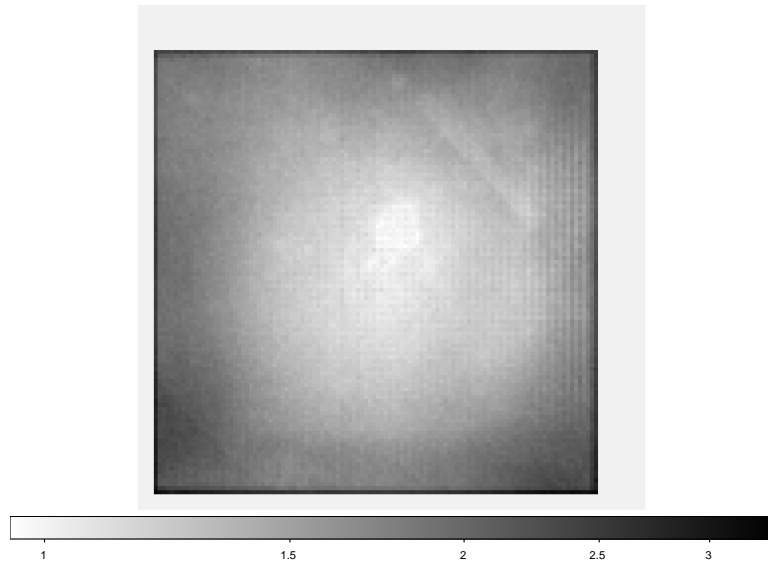


Figure 6: Pre-flight SAMP gain map (hrcID1998-10-30sampgainN0001.fits), shown on a log scale from 0.95 to 3.35.

For the previous set of maps, released in 2007, we calculated the temporal correction by fitting the PHAs with a simple linear function, excluding the first two data points from the fit (see Figure 3 in Posson-Brown & Kashyap 2007). Here, we take a different approach. First, we use the aimpoint

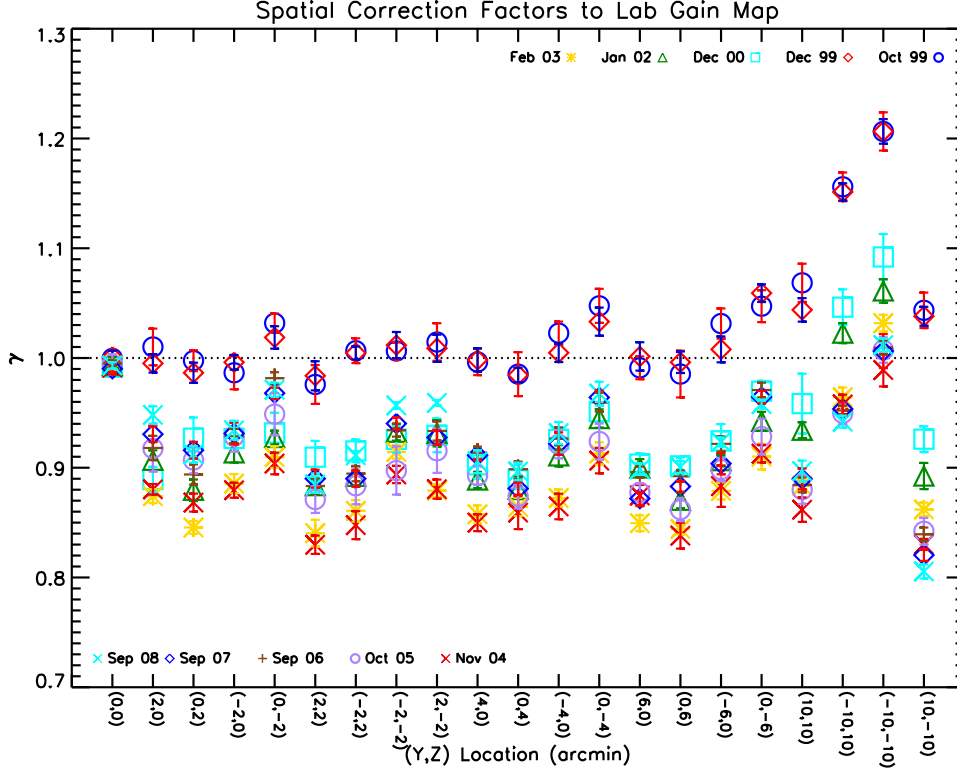


Figure 7: Spatial gain correction factors, relative to the aimpoint, for each epoch.

observations of AR Lac, HZ 43 and G21.5-0.9 to compute a set of temporal correction factors for each source by matching the $\text{SAMP}(\vec{0}|t)$ profiles of later observations to the $\text{SAMP}(\vec{0}|t)$ profile of the earliest observation (October 1999 for AR Lac and G21.5-0.9, February 2000 for HZ 43). This profile matching technique is similar to how we calculate the spatial correction factors in §4.2.

Next, we fit the three sets of temporal correction factors concurrently with an inverse exponential plus linear function fit,

$$TC(t) = \frac{a_0 + a_3}{a_0 e^{-a_1 t} + a_2 t + a_3}. \quad (6)$$

We find best-fit parameters of $a_0 = 30.27 \pm 153.42$, $a_1 = 3.37 \times 10^{-2} \pm 4.20 \times 10^{-3}$, $a_2 = -1.74 \times 10^{-1} \pm 8.87 \times 10^{-1}$, and $a_3 = 121.34 \pm 615.40$. (The large uncertainties on a_0 and a_3 are due to the degeneracy of these parameters.) This fit is shown in Figure 9, along with the set of temporal correction factors for each source and the linear correction function used for the previous set of gain maps.

To obtain the final gain correction maps, we multiply the previously derived “flat-fielded” gain map $g(\vec{x}|t)$ for each epoch by the value of the temporal correction function $TC(t)$ at the value of t corresponding to that epoch. These maps are the final product of our analysis and are shown in Figure 10. They will be released in the CALDB once `hrc_process_events` has been modified to use SAMP in place of PHA for calculating the pulse invariant values. Note that after this change, what we have referred to in this memo as “SPI” will be called “PI” in HRC-I event lists, replacing the old PHA-based PI.

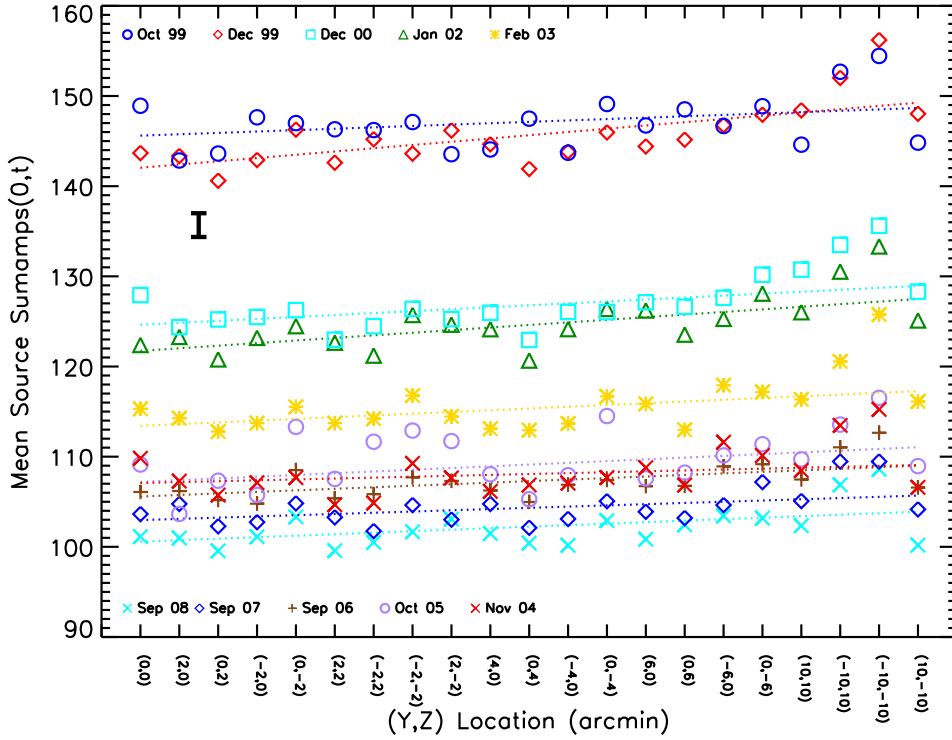


Figure 8: Mean “flat-fielded” SAMP values as a function of location on the detector, for all the AR Lac observations. The dashed lines show the best-fit line to each set.

4.4 Testing the New Maps

To test the new gain-correction maps, we return to the raw source and background SAMP values calculated from the Level 1 event lists. We convert the values to SPI using the appropriate map, then find the mean background-subtracted SPI.

Figure 11 shows the mean AR Lac SPI values as a function of observation location on the detector, with an error bar representing the average $\pm 1\sigma$ error. Comparing this figure to raw SAMPs versus location (Figure 5) and spatially-corrected SAMPs versus location (Figure 8), we can see that the new gain correction maps have performed their task: the spatial and temporal dependencies in pulse-height values have been removed. Figure 12 gives this information in a slightly different way, showing the residual differences in mean AR Lac SPI from the initial (October 1999) value at the aimpoint as a function of observation location.

We also test the new maps on the HZ 43 and G21.5-0.9 observations. Figures 13 and 14 show the mean SAMP and SPI values over time for these sources. PHA and PI are also shown for comparison. The gain decline over time is evident in both mean SAMP and PHA. The mean SPI values are systematically higher than mean PI, due to the differences in how the PHA and SAMP lab maps were normalized (§4.1).

5 Summary

To address the HRC-I gain decline, we have made a new set of time-dependent gain correction maps. This set differs from the set released in 2007 in that it is based on scaled SUMAMPS rather

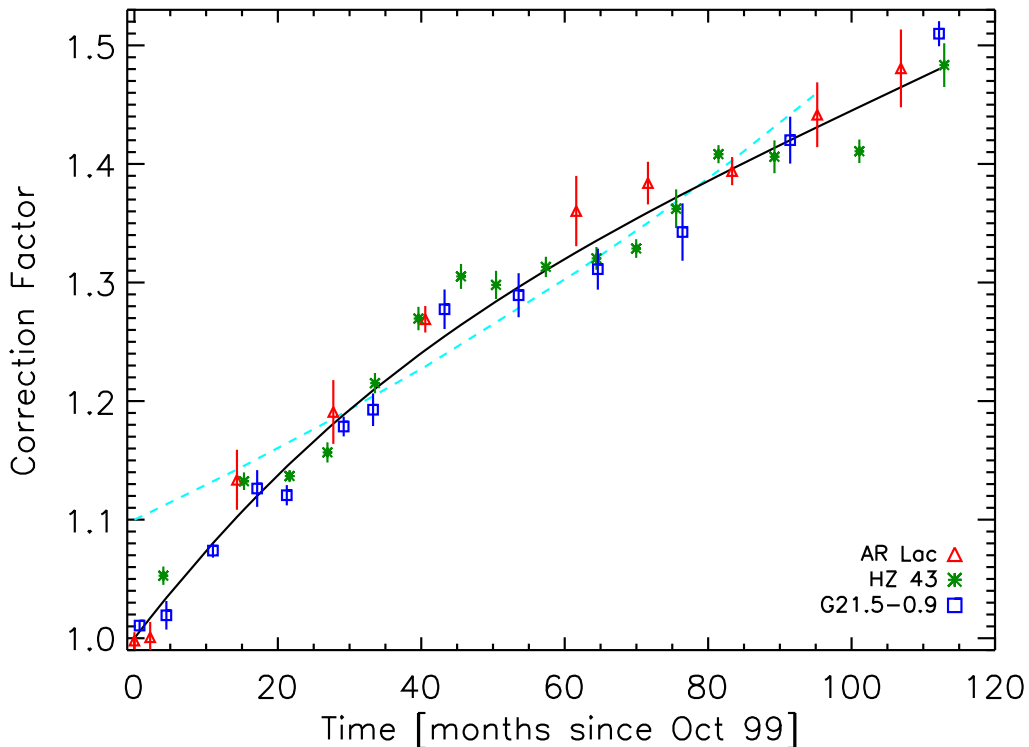


Figure 9: The temporal correction function $TC(t) = \frac{a_0 + a_3}{a_0 e^{-a_1 t} + a_2 t + a_3}$ (black line) fit to correction factors derived from AR Lac (red triangles), G21.5-0.9 (blue boxes) and HZ 43 (green asterisks) observations at the HRC-I aimpoint by matching the profile of later observations to the profile of the initial observation for each source. The dashed cyan line shows the temporal correction function that was used for the previous set of gain maps. Note that the new correction (black line) is continuous at time=0, whereas the previous one jumps from 1 at time=0 to 1.12. ($TC(0) = 1$ by definition.)

than PHA. (For both the HRC-I and HRC-S, the scaled sum of amplifier signals, SUMAMPS, is a better proxy for spectral response than the PHA.)

To make the gain correction maps, we model the spatial dependence of the gain change using observations of AR Lac taken yearly at the aimpoint and 20 offset locations on the detector. We derive a correction for the temporal dependence using aimpoint observations of AR Lac, HZ 43, and G21.5-0.9. The resulting time-dependent gain maps convert scaled SUMAMPS into "SUMAMPS pulse invariant" (SPI), allowing for comparison of source profiles taken at different epochs or locations on the detector.

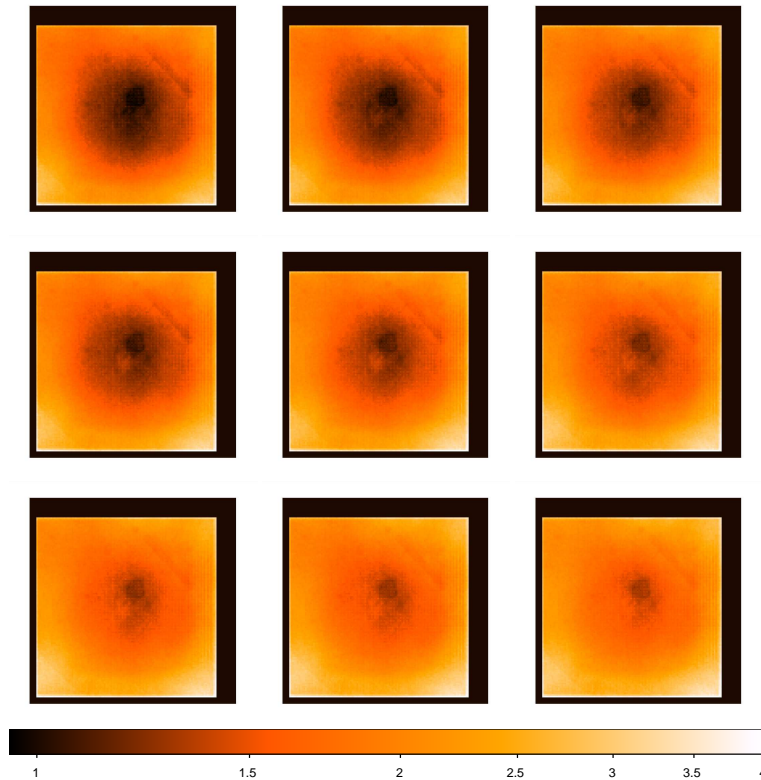


Figure 10: The final set of gain correction maps, shown on a log scale ranging 0.95-4.0. Top row (L->R): hrciD1999-10-04sampgainN0001.fits, hrciD2000-12-12sampgainN0001.fits, hrciD2002-01-26sampgainN0001.fits. Middle Row (L->R): hrciD2003-02-22sampgainN0001.fits, hrciD2004-11-25sampgainN0001.fits, hrciD2005-10-17sampgainN0001.fits. Bottom row (L->R): hrciD2006-09-20sampgainN0001.fits, hrciD2007-09-17sampgainN0001.fits, hrciD2008-09-07sampgainN0001.fits.

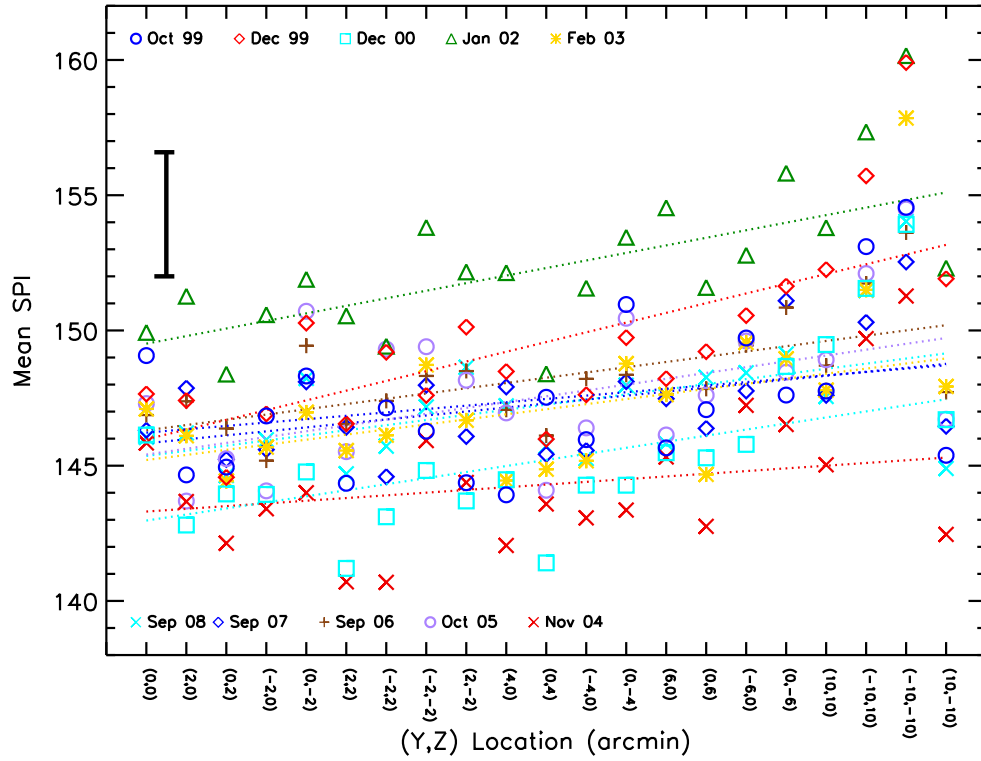


Figure 11: Mean SPI values for AR Lac with average $\pm 1\sigma$ error bar.

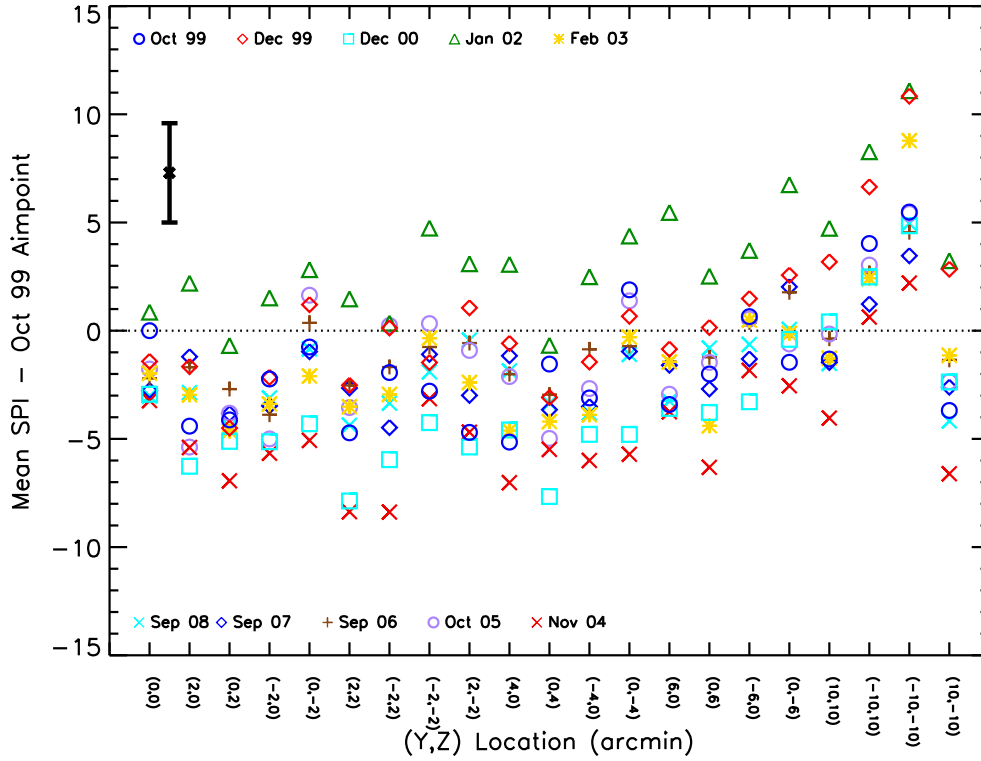


Figure 12: Mean SPI values for AR Lac with the Oct 99 aimpoint value subtracted. Error bar is $\pm 1\sigma$.

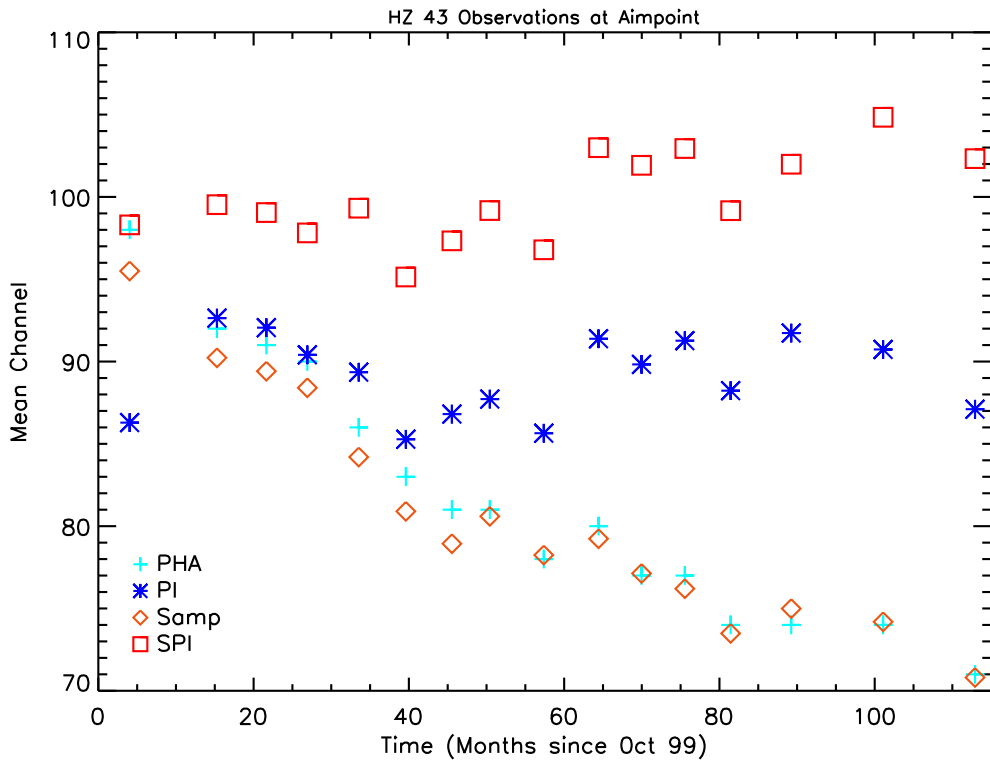


Figure 13: Mean SPI values for HZ 43 (red boxes), compared to mean SAMP values (orange diamonds), mean PHA (cyan crosses), and mean PI (blue asterisks).

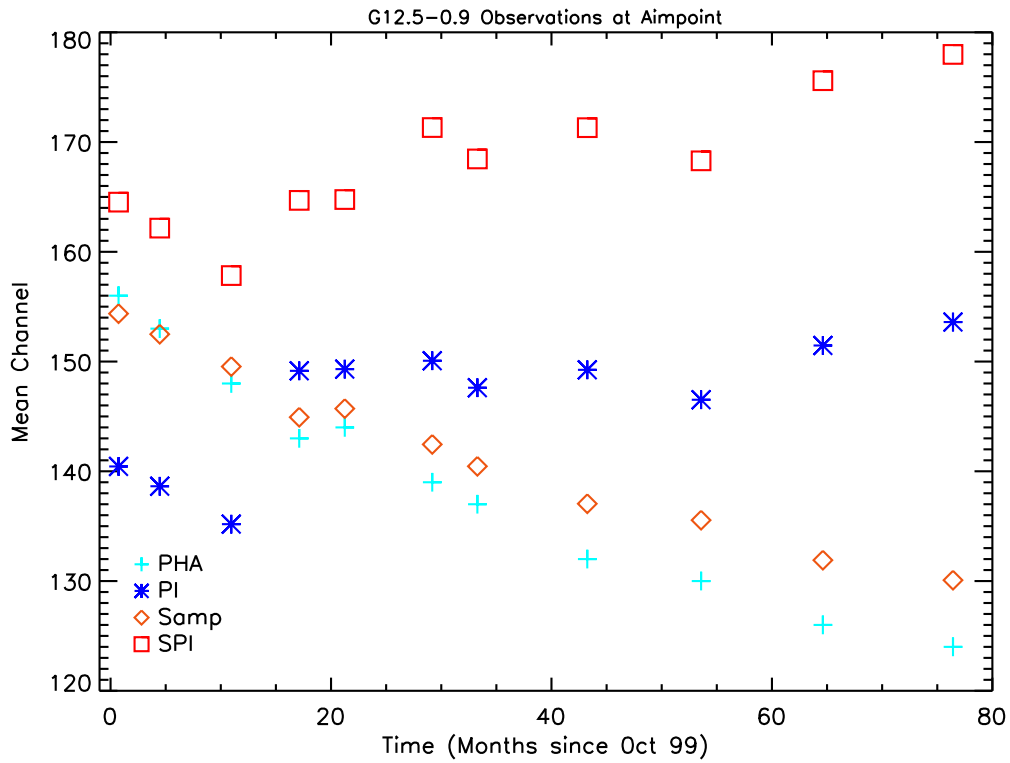


Figure 14: Mean SPI values for SNR G21.5-0.9 (red boxes), compared to mean SAMP values (orange diamonds), mean PHA (cyan crosses), and mean PI (blue asterisks).

References

- Kashyap V and Drake J J 2000, BASI 28, 475
- Posson-Brown J and Donnelly R H 2003, *Evolution of PHA Response in the HRC*, (CXC Memo, available at <http://asc.harvard.edu/cal/Hrc/gain.html>)
- Posson-Brown J and Kashyap V 2007, *HRC-I Gain Correction*, (CXC Memo, available at http://asc.harvard.edu/cal/Hrc/Documents/Gain/hrci_gain_correction.pdf)
- Posson-Brown J and Kashyap V 2009 *SUMAMPS-based gain maps and RMF for the HRC-I*, Poster #C.16 at the 2009 Chandra Calibration Review, available at http://cxc.harvard.edu/ccr/proceedings/09_proc/presentations/possonbrown2/
- Wargelin B J, Ratzlaff P W and Juda M 2008 *A New Gain Map and Pulse-Height Filter for the Chandra LETG/HRC-S Spectrometer*, (CXC Memo, available at <http://cxc.harvard.edu/cal/Letg/Gain/>)
- Wilton C, Posson-Brown J, Juda M and Kashyap V 2005 *The HRC-I Gain Map*, Poster #9.10 at the 2005 Chandra Calibration Workshop, available at http://asc.harvard.edu/ccw/proceedings/05_proc/presentations/wilton/

Table 1: HRC-I ARLac calibration observations used in creation of the time-dependent gain correction maps.

(Y, Z) Offset [arcmin]	Oct 99			Dec 99			Dec 00			Jan 02		
	ObsID	Exptime [s]	DTCOR									
(0,0)	1321	994.893	0.994	1484	1287.76	0.995	996	3079.97	0.996	2608	1187.59	0.994
(2,0)	1324	994.911	0.995	1485	1279.25	0.994	2345	1182.04	0.988	2617	1186.43	0.994
(0,2)	1342	994.932	0.995	1491	1288.67	0.995	2351	1180.02	0.995	2611	1186.41	0.994
(-2,0)	1336	992.810	0.994	1489	1293.24	0.998	2349	1184.09	0.995	2610	1193.82	0.994
(0,-2)	1330	994.854	0.994	1487	1279.34	0.995	2347	1177.71	0.993	2618	1189.64	0.994
(2,2)	1345	994.893	0.994	1492	1279.76	0.994	2352	1180.02	0.995	2604	1122.47	0.999
(-2,2)	1339	992.794	0.994	1490	1287.82	0.995	2350	1188.19	0.995	2619	1188.50	0.994
(-2,-2)	1333	994.878	0.994	1488	1287.83	0.995	2348	1177.97	0.995	2624	1658.56	0.995
(2,-2)	1327	994.768	0.994	1486	1286.66	0.995	2346	1182.04	0.993	2609	1188.50	0.994
(4,0)	1348	994.927	0.995	1493	1286.80	0.995	2353	1149.96	0.995	2620	1191.83	0.994
(0,4)	1366	994.908	0.995	1499	1286.95	0.995	2359	1189.98	0.995	2606	1197.72	0.994
(-4,0)	1360	994.983	0.995	1497	1286.74	0.995	2357	1189.99	0.995	2621	1186.68	0.994
(0,-4)	1354	994.912	0.995	1495	1288.72	0.995	2355	1177.94	0.995	2612	1193.78	0.994
(6,0)	1351	994.875	0.994	1494	1287.65	0.995	2354	1179.98	0.995	2605	1188.82	0.994
(0,6)	1369	994.901	0.995	1500	1289.40	0.995	2360	1188.90	0.995	2607	1186.77	0.994
(-6,0)	1363	994.946	0.995	1498	1287.84	0.995	2358	1180.00	0.995	2613	1188.64	0.994
(0,-6)	1357	993.032	0.995	1496	1289.85	0.995	2356	1165.67	0.995	2614	1188.62	0.994
(10,10)	1372	994.967	0.995	1501	1288.26	0.995	2361	1189.99	0.995	2615	1186.83	0.995
(-10,10)	1381	8145.72	0.993	1504	1284.88	0.995	2364	1179.96	0.995	2616	1195.73	0.995
(-10,-10)	1378	994.991	0.995	1503	1290.18	0.995	2363	1099.99	0.995	2623	1188.72	0.995
(10,-10)	1375	995.055	0.995	1502	1287.84	0.995	2362	1159.97	0.995	2622	1195.72	0.995
(Y, Z) Offset [arcmin]	Feb 03			Nov 04			Oct 05			Sep 06		
	ObsID	Exptime [s]	DTCOR									
(0,0)	4294	1176.86	0.994	6133	1076.92	0.993	5979	1970.90	0.992	6519	3143.17	0.991
(2,0)	4303	1179.68	0.994	6134	1071.80	0.993	5980	1045.48	0.884	6520	1173.98	0.991
(0,2)	4297	1179.68	0.994	6135	1079.14	0.993	5981	589.796	0.500	6521	1171.12	0.991
(-2,0)	4296	1175.69	0.995	5063	1059.93	0.993	5982	1061.43	0.896	6522	1175.34	0.991
(0,-2)	4304	1177.40	0.994	5064	1068.12	0.993	5983	410.867	0.349	6523	1165.13	0.991
(2,2)	4290	646.692	0.999	5066	1077.09	0.993	5985	539.020	0.457	6525	1169.15	0.991
(-2,2)	4305	1100.07	0.994	5067	1083.02	0.993	5986	383.852	0.323	6526	1172.19	0.991
(-2,-2)	4310	1553.98	0.995	5068	1073.57	0.993	5987	235.416	0.200	6527	1159.18	0.991
(2,-2)	4295	1178.42	0.995	5065	1083.07	0.993	5984	582.467	0.493	6524	1165.45	0.991
(4,0)	4306	1175.64	0.995	5071	1066.16	0.992	5990	1125.68	0.992	6530	1164.40	0.991
(0,4)	4293	1178.96	0.994	5073	1068.13	0.992	5992	1171.31	0.993	6532	1175.32	0.991
(-4,0)	4307	1179.66	0.994	5075	511.306	0.992	5994	1174.03	0.993	6534	1174.22	0.991
(0,-4)	4300	1178.63	0.994	5069	1076.88	0.993	5988	311.304	0.264	6528	1174.21	0.991
(6,0)	4291	886.898	0.991	5072	1066.25	0.992	5991	1166.76	0.993	6531	1171.18	0.991
(0,6)	4292	1175.26	0.994	5074	672.529	0.989	5993	1179.36	0.993	6533	1165.43	0.991
(-6,0)	4299	1182.44	0.994	5076	798.618	0.990	5995	1167.47	0.992	6535	1171.12	0.991
(0,-6)	4298	1173.10	0.994	5070	1077.90	0.993	5989	415.781	0.357	6529	1165.94	0.991
(10,10)	4301	1176.34	0.994	5079	1078.81	0.993	5998	1176.88	0.992	6538	1182.17	0.991
(-10,10)	4302	1173.44	0.994	5080	1073.95	0.993	5999	1164.38	0.992	6539	1174.40	0.991
(-10,-10)	4309	1182.73	0.995	5077	1061.77	0.992	5996	1058.72	0.989	6536	1172.21	0.991
(10,-10)	4308	1173.62	0.995	5078	1078.00	0.993	5997	1148.12	0.990	6537	1164.54	0.991

Table 2: HRC-I AR Lac calibration observations used in creation of the time-dependent gain correction maps, continued.

(Y, Z) Offset [arcmin]	Sep 07			Sep 08		
	ObsID	Exptime [s]	DTCOR	ObsID	Exptime [s]	DTCOR
(0,0)	8298	3143.10	0.989	9640	3150.30	0.989
(2,0)	8299	1175.68	0.989	9641	1345.41	0.989
(0,2)	8300	1169.66	0.989	9642	1349.71	0.989
(-2,0)	8301	1165.66	0.990	9643	1340.32	0.987
(0,-2)	8302	1169.67	0.990	9644	1346.59	0.988
(2,2)	8304	1171.71	0.990	9646	1353.74	0.989
(-2,2)	8305	1171.71	0.990	9647	1347.45	0.989
(-2,-2)	8306	1165.64	0.990	9648	1351.77	0.989
(2,-2)	8303	1177.82	0.990	9645	1342.10	0.987
(4,0)	8309	1175.79	0.990	9651	1345.70	0.989
(0,4)	8311	1173.81	0.990	9653	1351.52	0.989
(-4,0)	8313	1171.84	0.990	9655	1345.71	0.989
(0,-4)	8307	1177.84	0.990	9649	1345.71	0.989
(6,0)	8310	1169.53	0.990	9652	1353.72	0.989
(0,6)	8312	1167.76	0.990	9654	1351.85	0.989
(-6,0)	8314	1163.49	0.990	9656	1349.73	0.989
(0,-6)	8308	1167.69	0.990	9650	1351.82	0.989
(10,10)	8317	1173.93	0.990	9659	1347.55	0.989
(-10,10)	8318	1167.59	0.990	9660	1352.71	0.988
(-10,-10)	8315	1171.94	0.990	9657	1347.62	0.989
(10,-10)	8316	1169.69	0.990	9658	1355.87	0.989

Table 3: HRC-I HZ43 calibration observations used in creation of the time-dependent gain correction maps.

ObsID	Date	Exptime [s]	DTCOR
1514	2000-02-03	2147.29	0.994
1000	2001-01-12	3873.01	0.995
1001	2001-07-25	4940.32	0.994
2600	2002-01-02	1880.90	0.993
2602	2002-07-23	1877.54	0.992
3714	2003-01-24	1859.73	0.994
3715	2003-07-24	1883.86	0.994
5043	2003-12-20	1970.50	0.994
5045	2004-07-19	2133.10	0.993
5958	2005-02-20	2165.59	0.993
5960	2005-08-08	2128.83	0.980
6474	2006-01-25	2144.94	0.992
6476	2006-07-24	2168.56	0.991
8275	2007-03-19	2156.48	0.990
9619	2008-03-14	2161.89	0.990
10623	2009-03-11	2160.37	0.988

Table 4: HRC-I G21.5-0.9 calibration observations used in creation of the time-dependent gain correction maps.

ObsID	Date	Exptime [s]	DTCOR
1406	1999-10-25	29855.4	0.990
142	2000-02-16	30313.7	0.994
144	2000-09-01	30030.0	0.995
1555	2001-03-09	8932.91	0.995
1556	2001-07-13	10098.6	0.995
2867	2002-03-12	19076.3	0.994
2874	2002-07-15	19762.6	0.994
3694	2003-05-15	18293.5	0.994
5167	2004-03-25	19069.5	0.994
6072	2005-02-26	19020.2	0.993
6742	2006-02-21	20016.4	0.992
8373	2007-05-25	19985.9	0.990
10648	2009-02-17	10063.7	0.989